Nano Today 33 (2020) 100860

Contents lists available at ScienceDirect

Nano Today

journal homepage: www.elsevier.com/locate/nanotoday

Bio-inspired Nanoscaled Electronic/Ionic Conduction Networks for Room-Temperature All-Solid-State Sodium-Sulfur Battery

Hongli Wan[a,b], Wei Weng[a,b], Fudong Han[c], Liangting Cai[a], Chunsheng Wang[c,*], Xiayin Yao[a,b,**]

[a] Ningbo Institute of Materials Technology and Engineering, Chinese Academy of Sciences, Ningbo, 315201, PR China
[b] Center of Materials Science and Optoelectronics Engineering, University of Chinese Academy of Sciences, Beijing, 100049, PR China
[c] Department of Chemical and Biomolecular Engineering, University of Maryland, College Park, Maryland, 20742, United States

ARTICLE INFO

Article history:
Received 10 January 2020
Received in revised form 14 March 2020
Accepted 25 March 2020

Keywords:
All-solid-state sodium-sulfur battery
bio-inspired S-Na_3SbS_4-C cathode
nano-scaled electronic/ionic network
triple-phase interfacial contact
electrochemical performance

ABSTRACT

Sulfur cathode with nano-scaled electronic/ionic network is essential for all-solid-state Na/S batteries to achieve high energy density and long cycle life. However, it is great challenged to fabricate such a structure using either mechanical milling or liquid-phase reaction method. Here, a S-Na_3SbS_4-C cathode with distributed micro-scaled primary electronic/ionic highways along with nano-scaled secondary local-roads is fabricated by combining the liquid-phase reaction and mechanical milling. The formation mechanism for nano-scaled local-roads in S-Na_3SbS_4-C is systematically investigated. The S-Na_3SbS_4-C nanocomposite cathode with 3D distributed primary and secondary ionic/electronic conduction network provides a high initial discharge capacity of 1504.3 mAh g^{-1} at 50 mA g^{-1} with Coulombic efficiency of 98.5% at room temperature. Meanwhile, S-Na_3SbS_4-C/Na cells also demonstrate excellent rate capability with capacities of 1386.3, 1324.1, 1150.8, 893.4, 825.6, 771.2 and 662.3 mAh g^{-1} at current densities of 50, 100, 200, 300, 500, 1000 and 2000 mA g^{-1}, respectively. Even at ultrahigh cathode loading of 6.34 and 12.74 mg cm^{-2}, the S-Na_3SbS_4-C/Na cells can deliver reversible discharge specific capacities of 742.9 and 465.6 mAh g^{-1} at 100 mA g^{-1}, respectively. S-Na_3SbS_4-C/Na cell represents one of the best rate performances for room-temperature all-solid-state sodium-sulfur batteries reported to date. This work provides a simple strategy to design mixed conductive composite cathode for high-performance room-temperature all-solid-state sodium-sulfur batteries.

Introduction

Traditional sodium-sulfur batteries suffer from potential safety problem because the employment of molten sodium (anode) and sulfur (cathode) as electrodes in high operation temperature [1]. Room-temperature sodium-sulfur batteries have attracted intensive attention due to the improved safety, enhanced reliability and higher energy output [2]. However, room-temperature sodium-sulfur batteries using organic electrolytes suffer from low Coulombic efficiency and poor cycling stability, due to the low electronic conductivity of S and Na_2S, dissolution of sodium polysulfide, and large volume changes of S during charge-discharge processes [3,4]. To address these issues, carbon-sulfur [5–7] composite cathodes are used to improve the electron conducting property, ameliorate the volume change of sulfur and simultaneously trap sulfur on carbon to decrease the dissolution of polysulfide. Many porous carbons have been extensively investigated for S host, the shuttle effects still exist in almost all the liquid electrolyte based Na/S batteries. Employment of covalent sulfur [8] and confining small sulfur molecules in microporous carbon [9,10] can reduce the shuttle reaction, while the low S loading also reduce the total energy density of Na/S full cell.

All-solid-state sodium-sulfur battery can ultimately eliminate the shuttle reactions [11–13]. However, two main challenges that restrict the electrochemical performance of all-solid-state sodium-sulfur batteries are the low ionic conductivity of the electrolytes and the limited triple-phase contacts among active material, electrolytes and electronic additives. The low utilization of active materials caused by less and gradually reduced electronic/ionic conduction is one major challenge for all-solid-state battery, [14,15] because the volume expansion and contraction of active material during cycling reduces electrolyte/active mate-

* Corresponding author.
** Corresponding author at: Ningbo Institute of Materials Technology and Engineering, Chinese Academy of Sciences, Ningbo, 315201, PR China.
E-mail addresses: cswang@umd.edu (C. Wang), yaoxy@nimte.ac.cn (X. Yao).

https://doi.org/10.1016/j.nantod.2020.100860
1748-0132/

rial/carbon triple-boundaries. Inspired by excellent pipeline to transport water from the roots to the leaves in trees, the electronic/ionic conduction in cathodes should have the micro-scaled highway and then well-distribute into nano-scaled local-roads to ensure a large triple-phase boundary and achieve a high capacity and long cycle life. The two-level electronic/ionic transport system can be fabricated by synthesizing the nano-sized cathode material with nanoscaled electronic/ionic conduction network, then incorporate these composite cathode materials with micro-sized electronic/ionic conducting materials.

Several methods have been reported to synthesize such nanocomposite cathode. Co-precipitation from precursor solution with followed annealing is an efficient method to fulfill nano-scaled intimate electrolyte/active material interface because co-precipitated active material and the electrolyte after followed annealing process can form strongly bonded interface [16–18]. Using Li_2S-Li_6PS_5Cl-C nanocomposite [19] as a model cathode, we co-precipitate Li_2S active material and Li_6PS_5Cl electrolyte on polyvinylpyrrolidone carbon precursor. During the following high-temperature carbonization process, Li_2S and Li_6PS_5Cl with partial lattice match each other are anchored onto carbon surface ensuring large and robust triple interphase. The resultant all-solid-state lithium-sulfur battery delivered reversible capacity of 830 mA h g^{-1} at current density of 50 mA g^{-1} for 60 cycles. Fan *et al.* synthesized Na_2S-Na_3PS_4-CMK-3 nanocomposite cathode [12] through casting-annealing technology, which can realize strong interfacial contacts and eliminate the residential stress in Na_2S cathode, leading to an improved reversible capacity of 810 mA h g^{-1} under current density of 50 mA g^{-1} for 50 cycles at 60 °C. However, at a high current density of 150 mA g^{-1}, the battery only exhibits a capacity of 200 mA h g^{-1}, indicating the ionic conductivity of Na_3PS_4 electrolyte (3.45×10^{-4} S cm^{-1} at 60 °C) still restricts the overall electrochemical performance of all-solid-state sodium-sulfur batteries. However, co-precipitation and casting/annealing method cannot be employed to synthesize sulfur/electrolyte nanocomposite, because sulfur will sublimate during the annealing process. Herein, a self-forming nano-scaled ionic/electronic conduction networks in S-Na_3SbS_4-C composite cathode is fabricated by liquid-phase reaction and followed with ball-milling process to *in-situ* form uniformly nano-scale ionic/electronic conducting channel in cathode. In this method, ball-milling process replaces annealing process to transfer electrolyte precursor to Na_3SbS_4 electrolyte, which can eliminate the sublimation of sulfur and simultaneously decrease the particle size of active material.

Inspired by the efficient structure of biological systems and highway systems [20,21], these nano-scaled ionic/electronic conduction networks have to be connected by micro-sized high conducting stem to allow fast flow of ion and electron in all the direction of cathode. Therefore, S-Na_3SbS_4-C composite was further mixed with electronic conducting carbon and Na_3SbS_4 electrolyte with room temperature ionic conductivity of 1.14 mS cm^{-1} to realize high micro-scaled primary ionic/electronic conduction networks in the cathode layer (Fig. 1), thus leading to the resultant S-Na_3SbS_4-C/Na_3SbS_4/Na all-solid-state sodium-sulfur batteries exhibit excellent cycling stability and rate capability at room temperature.

Results and Discussion

Synthesis of S-Na_3SbS_4 composites

S-Na_3SbS_4 composites with nano-scaled ionic conduction channels were synthesized by liquid-phase reaction and followed with ball-milling process. Fig. 2a shows the synthesis process of S-Na_3SbS_4 composite. The formation mechanism of S-Na_3SbS_4 in the synthesis process was investigated using XRD and Raman. Firstly, Na_3SbS_4 precursor was prepared by mixing of Na_2S, Sb_2S_3 and S with mole ratio of 3:1:2 in acetonitrile. After stirring at 50 °C for different times, the precursor solution was distilled and further dried at 80 °C for 12 hours to remove the residual solvent. With increasing the stirring and reaction time, the Raman peaks for Na_2S and S gradually disappear, while the Raman peaks for sodium polysulfides gradually appears (Fig. S1). However, the XRD patterns for Sb_2S_3 still retain through the reaction process (Fig. S2). Therefore, after liquid-phase reaction and drying process, only the electrolyte precursor (Sb_2S_3 and sodium polysulfides) rather than Na_3SbS_4 electrolyte was formed. To form S-Na_3SbS_4 active material-electrolyte composite, $S_{active\ material}$ was added to formed electrolyte precursor (Sb_2S_3 and sodium polysulfides) and then ball-milling was applied to the mixtures. During ball-milling process, Sb_2S_3 and sodium polysulfides reacted to *in-situ* form Na_3SbS_4 electrolyte (Figs. S3, S4), and thus forming S-Na_3SbS_4 composite (Figs. S5, S6). However, if directly ball-milling the mixture of Na_2S, Sb_2S_3, $S_{electrolyte}$ and $S_{active\ material}$ together, impurities are always existed in the obtained composite (Fig. S7). Therefore, two step reaction of liquid-phase and ball-milling are essential for synthesis of S-Na_3SbS_4 composites.

Since Sb_2S_3 does not involve the liquid reaction in the synthesis of electrolyte precursor, alternatively S-Na_3SbS_4 electrolyte can also be synthesized by mixing Na_2S and $S_{electrolyte}$ with mole ratio of 3:2 (without Sb_2S_3) in ACN for 24 h, and then ball-milling the obtained Na_2S_2, Na_2S_4 and Na_2S (Fig. S8) with Sb_2S_3 and $S_{active\ material}$ (Fig. S9). Therefore, Sb_2S_3 can be added either in the first step liquid-phase reaction or in the late ball-milling procedure. However, if Na_2S, $S_{electrolyte}$ and $S_{active\ material}$ were firstly mixed in ACN, Na_2S_4 and unreacted sulfur were detected in the XRD pattern (Fig. S10). Further ball-milling the produced mixture with Sb_2S_3, some impurities were observed in the synthesized S-Na_3SbS_4 composite (method 3, Fig. S11).

In summary, for preparing Na_3SbS_4 electrolytes, Na_2S and S should react to form sodium polysulfides through liquid-phase reaction in acetonitrile, and then Sb_2S_3 will react with sodium polysulfides during ball-milling process to obtain the final Na_3SbS_4 electrolyte (Fig. 2b). However, when changing reaction solvent to dimethoxyethane, impurities will be observed in the final Na_3SbS_4 electrolyte (Fig. S12). For synthesizing S-Na_3SbS_4 composite, the Sb_2S_3 and polysufides was firstly formed in the liquid-phase reaction, and then ball-milled with $S_{active\ material}$ to form S-Na_3SbS_4 composite (Fig. 2c).

Synthesis of S-Na_3SbS_4-C composites

In S-Na_3SbS_4 composite, the nano-scaled ionic conduction pathway was *in-situ* formed. However, the electronic conduction is absent, which will restrict the electrochemical performance of the as-prepared composite. Carbon was further introduced into the composite cathode to construct electronic network (Fig. 3a). After ball-milling $S_{active\ material}$, Na_3SbS_4 electrolyte precursor and Super P with weight ratio of 1.2: 2.0: 0.4, S-Na_3SbS_4-C composite ($S_{1.2}E_{2.0}C_{0.4}$) was obtained. x, y, z in $S_xE_yC_z$ denotes the weight ratio of $S_{active\ material}$, Na_3SbS_4 electrolyte precursor and Super P. The existence of S in S-Na_3SbS_4-C composite (Fig. 3b) is evidenced by XRD diffraction peaks at 23.06°, 26.70°, 27.69°, 28.65°, 31.38° and 37.03° (JCPDS: #24-0733). The remaining peaks at 17.48°, 24.82°, 30.52°, 35.38°, 39.72°, 43.70°, 47.40°, 50.90°, 57.44°, 63.52° and 66.44° are ascribed to cubic Na_3SbS_4 (JCPDS: #30-1154). Raman spectroscopy (Fig. 3c) was conducted to further confirm the composition of S-Na_3SbS_4-C composite. Sulfur shows sharp characteristic peaks at 155, 222, and 473 cm^{-1}, which derives from the bending and the stretching of S–S bonds [22], respectively. The peaks at 360 cm^{-1} and 384 cm^{-1} assign to the stretching vibration modes

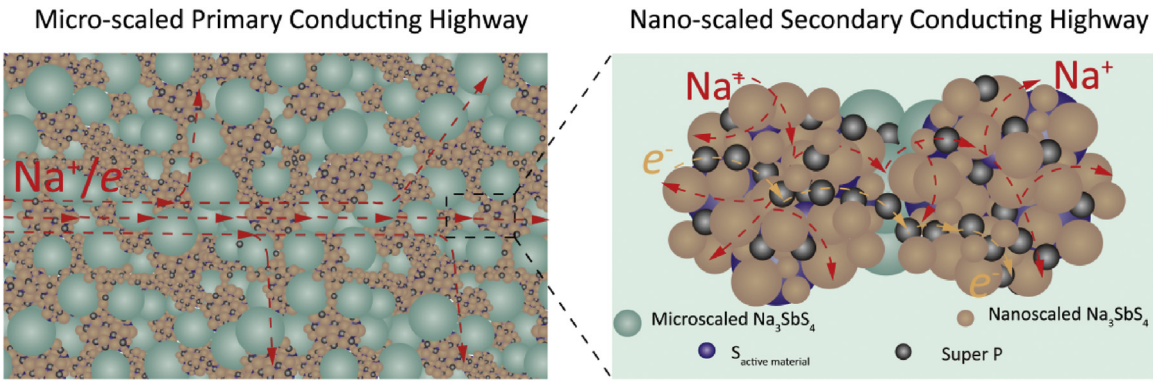

Fig. 1. Illustration of the ionic/electronic conducting channels in S-Na_3SbS_4-C composite based cathode.

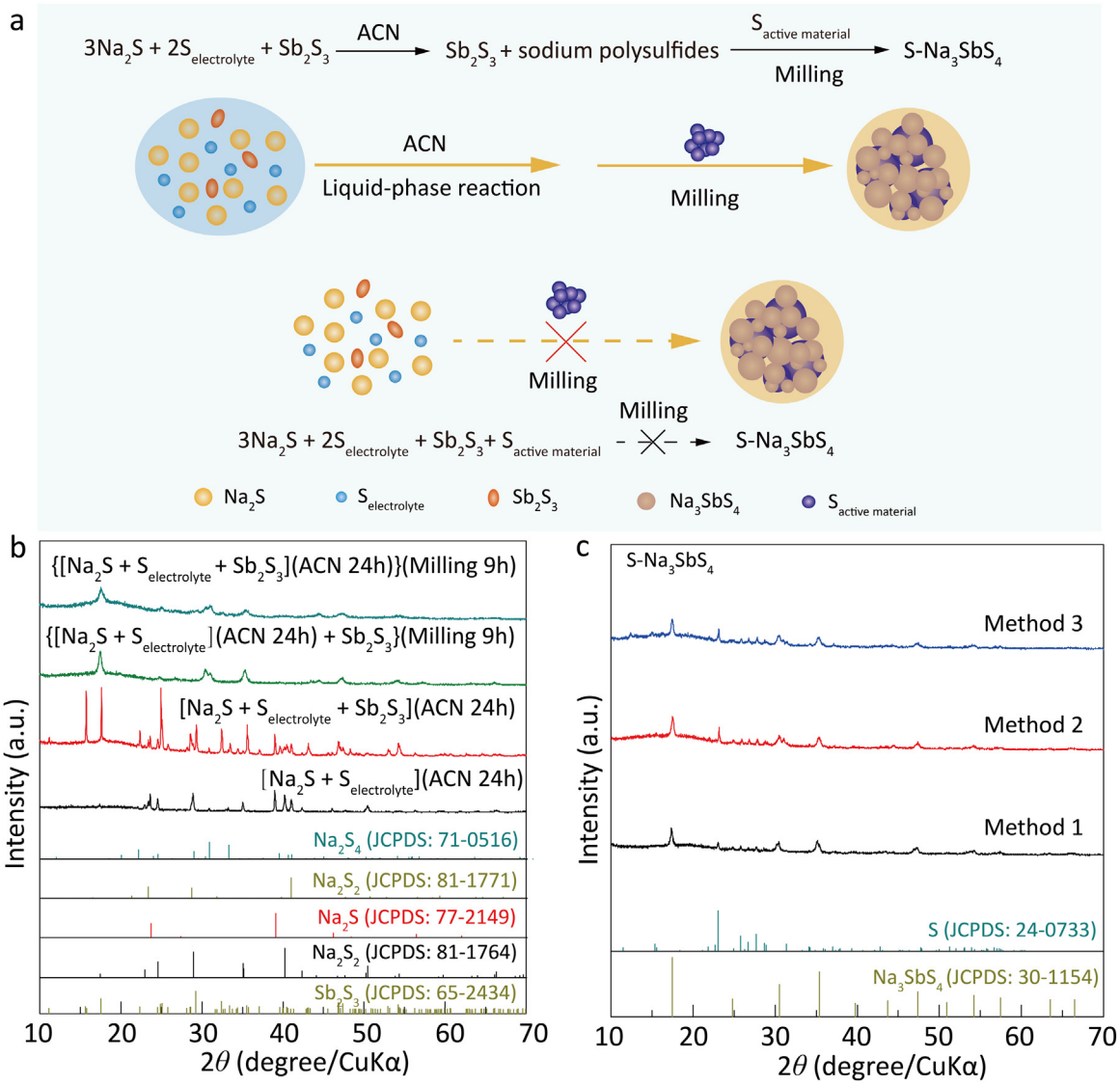

Fig. 2. a) Reaction pathway and formation mechanism for S-Na_3SbS_4 composite, b) XRD pattern of Na_3SbS_4 electrolyte synthesized by different routes, c) XRD pattern of S-Na_3SbS_4 composite synthesized by different methods.

of Sb–S [23] in Na_3SbS_4 electrolyte. Peaks of 1350 cm^{-1} and 1585 cm^{-1} in Raman spectroscopy are attributed to D band and G band of Super P, which is related to the defects and disorder in hexagonal graphitic layers, and the vibration of the sp^2-bonded carbon atoms, respectively [24]. $S_{1.2}E_{2.0}C_{0.4}$ composite exhibits higher intensity ratio of D versus G band (I_D/I_G = 1.05) compared with that for Super P (I_D/I_G = 0.96) because of the structural distortion, indicating interaction was occurred between carbon and sulfur, which will enhance the electronic conductivity to accelerate the electron transport [25,26]. Fig. 3d-e shows the morphology of $S_{1.2}E_{2.0}C_{0.4}$

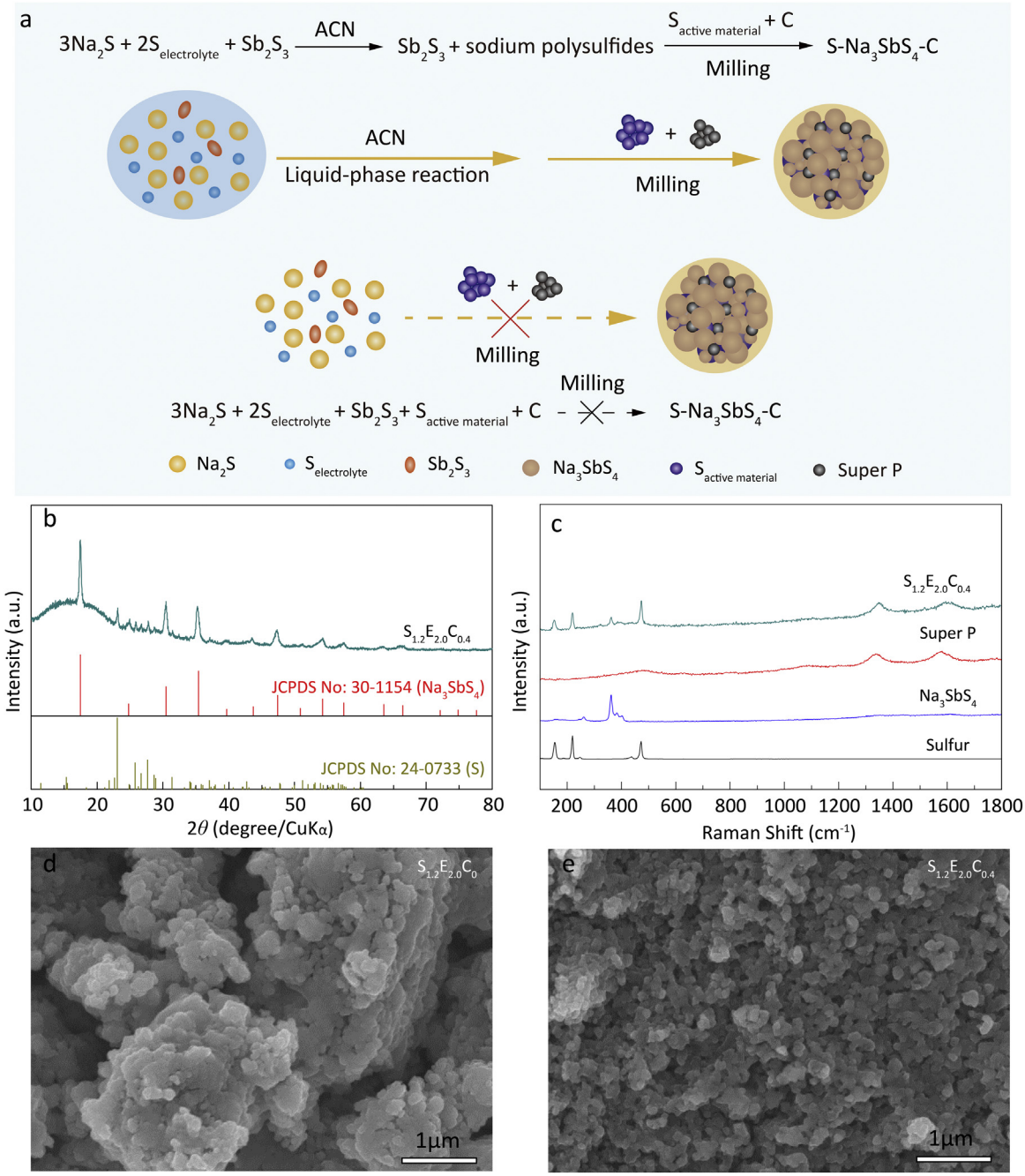

Fig. 3. a) Illustration of formation mechanism of S-Na_3SbS_4-C composite. b) XRD patterns of $S_{1.2}E_{2.0}C_0$ and $S_{1.2}E_{2.0}C_{0.4}$ composite, c) Raman spectra of $S_{1.2}E_{2.0}C_{0.4}$, Super P, Na_3SbS_4 electrolyte and sulfur, SEM images of d) $S_{1.2}E_{2.0}C_0$ and e) $S_{1.2}E_{2.0}C_{0.4}$.

and $S_{1.2}E_{2.0}C_0$ composites. Severe aggregation is clearly observed in $S_{1.2}E_{2.0}C_0$ composite (Fig. 3d), while, the particles were uniformly distributed throughout the $S_{1.2}E_{2.0}C_{0.4}$ composite and the particle size was reduced to around 200 nm (Fig. 3e). The particle size of $S_{1.2}E_{2.0}C_{0.4}$ composite is larger than that of Super P (~50 nm, Fig. S13), indicating sulfur, Super P and Na_3SbS_4 electrolyte were mixed together to form a secondary particle.

The structure of $S_{1.2}E_{2.0}C_{0.4}$ composite was further analyzed using transmission electron microscope (TEM) and high-resolution transmission electron microscopy (HRTEM). As shown in Fig. 4a, the $S_{1.2}E_{2.0}C_{0.4}$ composite with particle size of about 200 nm are homogeneously distributed without aggregation, which is in consistent with the SEM. In Fig. 4b, Super P shows both amorphous areas and regions of graphite layers with interlayer spacing of 0.350 nm attributed to (0 0 2) plane of graphite [24]. Other obvious lattice fringe of about 0.345 nm corresponds to (0 2 6) lattice plane of sublimed sulfur, and lattice fringe of about 0.358 nm can be indexed to (2 0 0) lattice plane of Na_3SbS_4 electrolytes. Furthermore, the STEM images in Fig. 4c confirm that element sulfur, carbon, sodium and antimony are perfectly overlapped in the composite, indicating the formation of close triple-phase contacts among sulfur/carbon/Na_3SbS_4 electrolyte. Therefore, all the carbon, sulfur and Na_3SbS_4 components in S-Na_3SbS_4-C composite are interconnected forming an integrated ionic/electronic conducting network (Figs. S14, S15) with a high electronic conductivity of 8.5×10^{-3} S cm^{-1} (Fig. S14). The realized ideal interfacial contacts and large triple-phase will significantly reduce the interfacial resistance and minimize the residential stress due

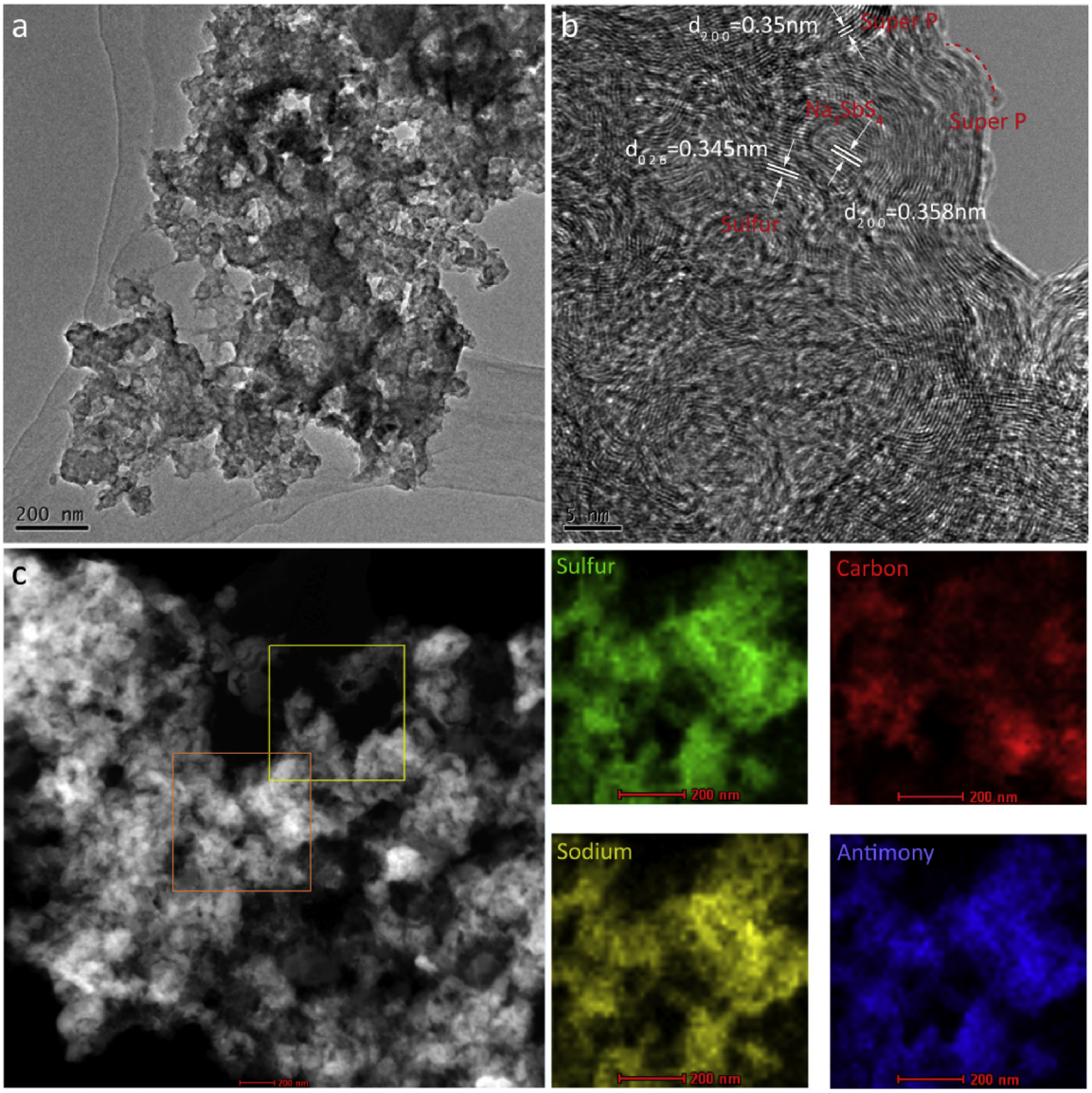

Fig. 4. a) TEM, b) HRTEM images and c) STEM spectra of $S_{1.2}E_{2.0}C_{0.4}$ composite (marked by the orange rectangle region).

to uniform volume change of sulfur during electrochemical process.

Fabrication and Electrochemical performance of $S_{1.2}E_{2.0}C_{0.4}$ cathodes with micro- and nano-scaled ionic/electronic conduction channels

To achieve a high performance, a primary electronic/ionic highway is also required to connect $S_xE_yC_z$ ($S_{1.2}E_{2.0}C_{0.8}$, $S_{1.6}E_{2.0}C_{0.4}$ and $S_{1.6}E_{2.0}C_{0.8}$) composites with nano-scaled balanced ionic/electronic conductivity together forming 3D efficiently distributed electronic/ionic channels for sulfur active materials. We optimized high and balanced primary electronic/ionic highway by optimizing the ratio of $S_xE_yC_z$, Na_3SbS_4 electrolyte and carbon in cathodes at 7: 2: 1 (Fig. S16). All the performance measurement of the $S_xE_yC_z$ (S-Na_3SbS_4-C) cathodes was conducted at room temperature in all-solid-state sodium battery within the cut-off voltage of 1.0 ~2.8 V using metallic sodium as anode and Na_3SbS_4 as electrolyte. Within this voltage range, the electrolyte is stable against sodium (Fig. S17) and the capacity contribution from the sulfide electrolyte is negligible (Fig. S18). The Na_3SbS_4 electrolyte with tetragonal structure (Fig. S19) has a total ionic conductivity of 1.14 mS cm^{-1} with Na^+ transference number of ~1.0 (Figs. S20, S21) at room temperature, ensuring fast ionic transportation in the electrolyte layer and inside cathode. Even though the XRD pattern (Fig. S22) for $S_{1.2}E_{2.0}C_{0.8}$, $S_{1.6}E_{2.0}C_{0.4}$ and $S_{1.6}E_{2.0}C_{0.8}$ composites is similar to $S_{1.2}E_{2.0}C_{0.4}$, the electrochemical performance of all the cathodes (Fig. S23) mentioned above is still inferior to that of $S_{1.2}E_{2.0}C_{0.4}$, which might be caused by the aggregation of the component material (Fig. S24) and concentrated strain/stress during charge/discharge process.

Fig. 5a shows the CV curves for $S_{1.2}E_{2.0}C_{0.4}$/Na_3SbS_4/Na all-solid-state sodium battery. A broaden reduction peak in the range of 1.0 ~ 1.7 V is related to the reduction of sulfur to Na_2S. In the anodic cycle, the oxidation peaks at 2.2 V and 2.4 V attribute to the multi-step conversion reaction of Na_2S to sulfur. For the following two cycles, the CV curves are similar to the first curve, indicating identical electrochemical reactions occur in the as-prepared $S_{1.2}E_{2.0}C_{0.4}$ cathode. Fig. 5b displays the first three charge-discharge voltage profile of $S_{1.2}E_{2.0}C_{0.4}$ cathode at room temperature in all-solid-state sodium-sulfur battery at 50 mA g^{-1}. A high initial discharge capacity of 1504.3 mAh g^{-1} (based on the mass of sulfur) with a ultrahigh Coulombic efficiency of 98.5% is delivered, which is

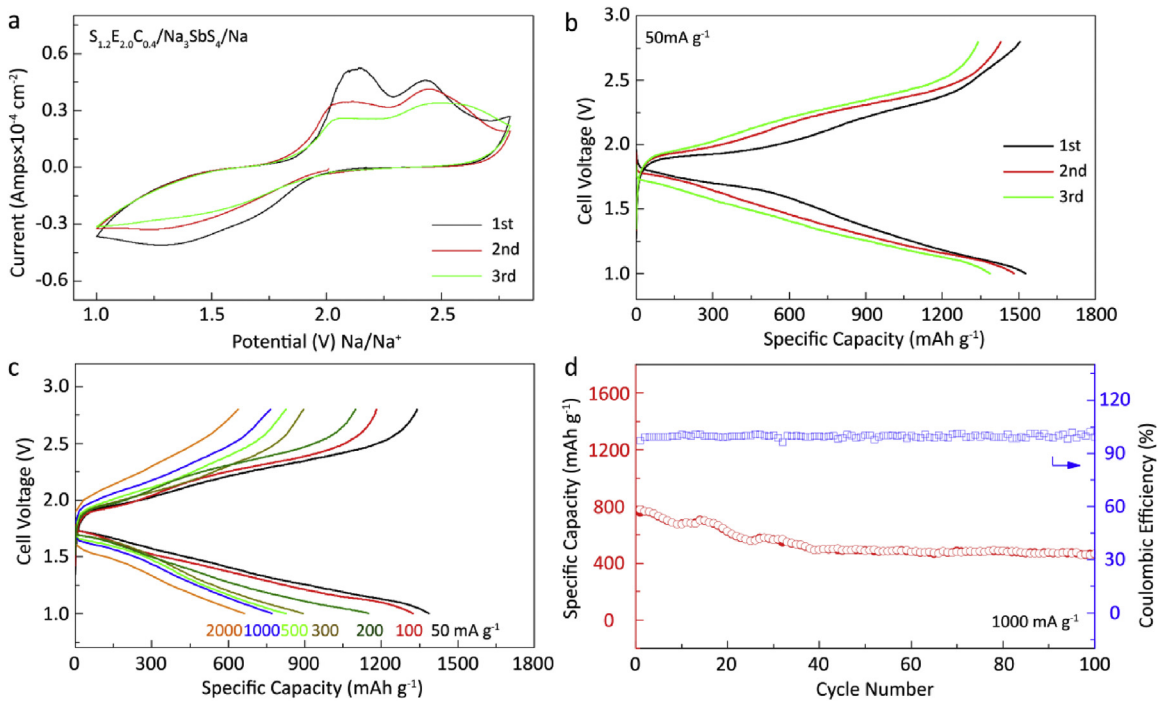

Fig. 5. a) CV curves of $S_{1.2}E_{2.0}C_{0.4}/Na_3SbS_4/Na$ all-solid-state sodium-sulfur battery, b) Galvanostatic discharge/charge profiles of $S_{1.2}E_{2.0}C_{0.4}/Na_3SbS_4/Na$ all-solid-state sodium-sulfur battery at 50 mA g^{-1} and room temperature, c) Galvanostatic discharge/charge profiles of the battery under different current densities at room temperature, d) Room-temperature cycling performance of the battery at current density of 1000 mA g^{-1}.

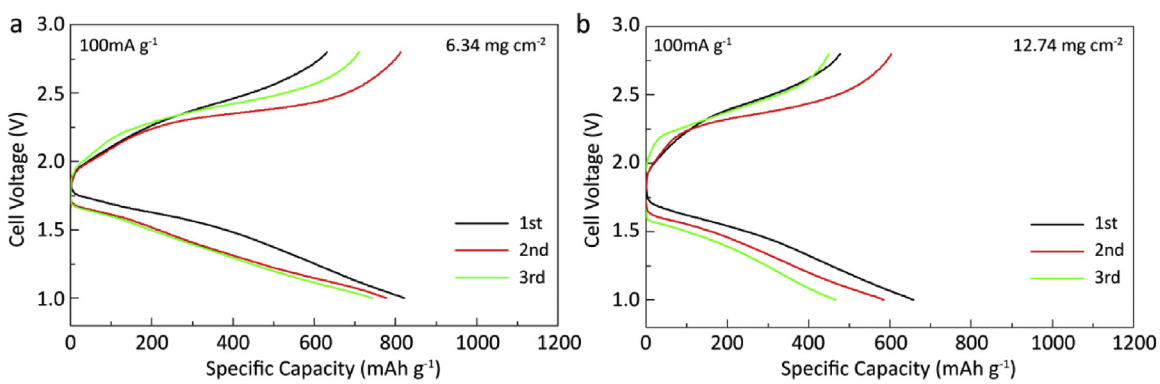

Fig. 6. Galvanostatic discharge/charge profiles of room-temperature $S_{1.2}E_{2.0}C_{0.4}/Na_3SbS_4/Na$ all-solid-state sodium-sulfur battery with cathode loading of a) 6.34 mg cm^{-2} and b) 12.74 mg cm^{-2}.

much higher than that of sodium-sulfur battery with organic liquid electrolytes [5,10,27]. In sharp contrast, the composite cathode employing directly mixed element sulfur, Na_3SbS_4 electrolyte and Super P only shows capacity of 691.9 mAh g^{-1} with much lower Coulombic efficiency of 40.2% (Fig. S25). The high capacity and Coulombic efficiency of $S_{1.2}E_{2.0}C_{0.4}$ cathode could benefit from the realization of nanoscaled triple-phase contacts. The rate capability of $S_{1.2}E_{2.0}C_{0.4}$ cathode was evaluated under different current densities at third cycle. As shown in Fig. 5c, the battery can deliver capacities of 1386.3, 1324.1, 1150.8, 893.4, 825.6, 771.2 and 662.3 mAh g^{-1} at current densities of 50, 100, 200, 300, 500, 1000 and 2000 mA g^{-1}, respectively. Fig. 5d displays the high rate cycling stability of the battery at current density of 1000 mA g^{-1}. After cycling for 100 cycles, high discharge capacities of 468.1 mAh g^{-1} were maintained. The superior electrochemical performance of $S_{1.2}E_{2.0}C_{0.4}$ composite further demonstrates the realization of intimate triple-phase contacts and the construction an integrated ionic/electronic conducting pathway in the cathode, which can accommodate the stress/strain accumulation as well as maintain the structural integrity of electrode material during charge-discharge process [28].

The effect of sulfur loading on the electrochemical performances of $S_{1.2}E_{2.0}C_{0.4}$ composite cathode was also investigated. Room-temperature all-solid-state sodium-sulfur battery with high cathode loading of 6.34 and 12.74 mg cm^{-2} (Fig. 6) deliver a high reversible capacities of 742.9 mAh g^{-1} and 465.6 mAh g^{-1} at 100 mA g^{-1} after three cycles, respectively, which is hard to realize in the conventional sodium-sulfur battery using organic electrolyte.

Conclusions

A S-Na_3SbS_4-C with nanoscaled secondary electronic/ionic conducting networks with intimate triple contacts in the composite is successfully prepared by a mechanochemical process. All-solid-state sodium-sulfur batteries using S-Na_3SbS_4-C as cath-

ode deliver a high reversible capacity of 468.1 mAh g^{-1} after cycling at current density of 1000 mA g^{-1} for 100 cycles at room temperature. Besides, even at ultrahigh cathode loading of 6.34 and 12.74 mg cm^{-2}, the batteries can still deliver reversible discharge specific capacities of 742.9 and 465.6 mAh g^{-1} at 100 mA g^{-1}, respectively. The superior electrochemical performances of the room-temperature all-solid-state sodium-sulfur battery can be attributable to the stable interfacial contacts and reduced stress/strain in the cathode material. This work opens up a facile method for construction of high-performance cathode material in room-temperature all-solid-state sodium-sulfur battery.

CRediT authorship contribution statement

Hongli Wan: Conceptualization, Methodology, Validation, Investigation, Resources, Writing - original draft. **Wei Weng:** Resources, Investigation. **Fudong Han:** Writing - original draft, Validation. **Liangting Cai:** Methodology, Resources. **Chunsheng Wang:** Conceptualization, Methodology, Writing - original draft. **Xiayin Yao:** Conceptualization, Methodology, Writing - original draft, Supervision, Funding acquisition.

Declaration of Competing Interest

The authors declare that they have no conflicts of interest.

Acknowledgements

The work was supported by funding from the National Key R&D Program of China (Grant No. 2018YFB0905400), National Natural Science Foundation of China (Grant No. 51872303, U1964205), Zhejiang Provincial Natural Science Foundation of China (Grant No. LD18E020004, LY18E020018) and Youth Innovation Promotion Association CAS (2017342).

Appendix A. Supplementary data

Supplementary material related to this article can be found, in the online version, at doi:https://doi.org/10.1016/j.nantod.2020.100860.

References

[1] X.C. Lu, G.G. Xia, J.P. Lemmon, Z.G. Yang, J. Power Sources 195 (2010) 2431–2442.
[2] D. Zhou, Y. Chen, B.H. Li, H.B. Fan, F.L. Cheng, D. Shanmukaraj, T. Rojo, M. Armand, G.X. Wang, Angew. Chem. Int. Edit. 57 (2018) 10168–10172.
[3] A. Manthiram, X.W. Yu, Small 11 (2015) 2108–2114.
[4] J. Park, S.-H. Yu, Y.-E. Sung, Nano Today 18 (2018) 35–64.
[5] Q.Q. Lu, X.Y. Wang, J. Cao, C. Chen, K.N. Chen, Z.F. Zhao, Z.Q. Niu, J. Chen, Energy Storage Mater. 8 (2017) 77–84.
[6] R. Carter, L. Oakes, A. Douglas, N. Muralidharan, A.P. Cohn, C.L. Pint, Nano Lett. 17 (2017) 1863–1869.
[7] L. Hu, Y. Lu, T.W. Zhang, T. Huang, Y.C. Zhu, Y.T. Qian, ACS Appl. Mater. Interfaces 9 (2017) 13813–13818.
[8] L. Fan, R.F. Ma, Y.H. Yang, S.H. Chen, B.G. Lu, Nano Energy 28 (2016) 304–310.
[9] Y.X. Wang, J. Yang, W. Lai, S.L. Chou, Q.F. Gu, H.K. Liu, D. Zhao, S.X. Dou, J. Am. Chem. Soc. 138 (2016) 16576–16579.
[10] S. Xin, Y.X. Yin, Y.G. Guo, L.J. Wan, Adv. Mater. 26 (2014) 1261–1265.
[11] N. Tanibata, M. Deguchi, A. Hayashi, M. Tatsumisago, Chem. Mater. 29 (2017) 5232–5238.
[12] X.L. Fan, J. Yue, F.D. Han, J. Chen, T. Deng, X.Q. Zhou, S. Hou, C.S. Wang, ACS Nano 12 (2018) 3360–3368.
[13] J. Yue, F.D. Han, X.L. Fan, X.Y. Zhu, Z.H. Ma, J. Yang, C.S. Wang, ACS Nano 11 (2017) 4885–4891.
[14] C.-Z. Zhao, B.-C. Zhao, C. Yan, X.-Q. Zhang, J.-Q. Huang, Y. Mo, X. Xu, H. Li, Q. Zhang, Energy Storage Mater. 24 (2020) 75–84.
[15] M. Shin, A.A. Gewirth,Adv. Energy Mater. (2019), 1900938.
[16] X.Y. Yao, D. Liu, C.S. Wang, P. Long, G. Peng, Y.-S. Hu, H. Li, L.Q. Chen, X.X. Xu, Nano Lett. 16 (2016) 7148–7154.
[17] Q. Zhang, J.P. Mwizerwa, H.L. Wan, L.T. Cai, X.X. Xu, X.Y. Yao, J. Mater. Chem. A 5 (2017) 23919–23925.
[18] H.L. Wan, J.P. Mwizerwa, X.G. Qi, X. Liu, X.X. Xu, H. Li, Y.-S. Hu, X.Y. Yao, ACS Nano 12 (2018) 2809–2817.
[19] F.D. Han, J. Yue, X.L. Fan, T. Gao, C. Luo, Z.H. Ma, L.M. Suo, C.S. Wang, Nano Lett. 16 (2016) 4521–4527.
[20] S.-H. Lee, V. Sridhar, J.-H. Jung, K. Karthikeyan, Y.-S. Lee, R. Mukherjee, N. Koratkar, I.-K. Oh, ACS Nano 7 (2013) 4242–4251.
[21] Y. Zhang, P.H. Chen, X. Gao, B. Wang, H. Liu, H. Wu, H.K. Liu, S.X. Dou, Adv. Funct. Mater. 26 (2016) 7754–7765.
[22] X.Y. Yao, N. Huang, F.D. Han, Q. Zhang, H.L. Wan, J.P. Mwizerwa, C.S. Wang, X.X. Xu,Adv. Energy Mater. 7 (2017), 1602923.
[23] L. Zhang, D.C. Zhang, K. Yang, X.L. Yan, L.M. Wang, J.L. Mi, B. Xu, Y.M. Li,Adv. Sci. 3 (2016), 1600089.
[24] C.-M. Wu, P.-I. Pan, Y.-W. Cheng, C.-P. Liu, C.-C. Chang, M. Avdeev, S.-k. Lin, J. Power Sources 340 (2017) 14–21.
[25] T.H. Hwang, D.S. Jung, J.S. Kim, B.G. Kim, J.W. Choi, Nano Lett. 13 (2013) 4532–4538.
[26] W. Li, M. Zhou, H.M. Li, K.L. Wang, S.J. Cheng, K. Jiang, Energy Environ. Sci. 8 (2015) 2916–2921.
[27] S.Y. Wei, S.M. Xu, A. Agrawral, S. Choudhury, Y.Y. Lu, Z.Y. Tu, L. Ma, L.A. Archer, Nat. Commun. 7 (2016) 11722.
[28] K.T. Lee, J. Cho, Nano Today 6 (2011) 28–41.